Observation of avalanche-like transport during the power degradation of confinement in Heliotron J

[1,*]F. Kin, [1]S. Inagaki, [1]K. Nagasaki, [2]M. Luo, [1]T. Minami, [1]S. Ohshima, [1]S. Kobayashi, [1]S. Kado, [1]S. Konoshima, [1]T. Mizuuchi and [3]N. Marushchenko

[1]Institute of Advanced Energy, Kyoto University, Uji 611-0011, Japan
[2]Graduate School of Energy Science, Kyoto University, Uji 611-0011, Japan
[3]Max-Planck-Institut für Plasmaphysik, EURATOM Association, D-17491 Greifswald, Germany

*Corresponding author

Abstract

The power degradation of confinement is a common feature in heliotron/stellarator and tokamak plasmas. In this study, we observed avalanche-like electron thermal transport in Heliotron J under plasma conditions that exhibit power degradation against to the central Electron Cyclotron Heating (ECH). The newly installed GHz sampling Electron Cyclotron Emission (ECE) diagnostic provides the observation of long-radial propagation of electron temperature fluctuations. We found that the electron temperature fluctuations are associated with avalanches, because the T_e fluctuations (i) propagate from core to the edge with the speed comparable to the diamagnetic drift velocity, (ii) exhibit with a *1/f* power-law scaling in the frequency spectrum and a Hurst exponent close to 1, and (iii) dominate in the ECH deposition location and spread to the edge as the heating power increases. The time scale of avalanches is much faster than the diffusive transport, and the simple estimate of avalanche-driven electron heat flux accounts for a significant amount. Furthermore, the avalanches can spread to the SOL regime when they are enhanced, i.e., the T_e fluctuations correlate to the D_α emission, which also has a spectrum scaling with the *1/f* power-law.

1. Introduction

In magnetic confinement plasmas, the global energy confinement time (τ_E) scales to the heating power (P) as $\tau_E \propto P^{-0.6\pm0.1}$, which is called as power degradation of confinement [1,2]. Because the confinement degradation occurs across many devices including both tokamaks and heliotron/stellarators, the underlying physics can be considered as a fundamental transport mechanism. Thanks to a lot of works, the turbulent transport has been found as the most dominant transport process in hot confinement plasmas. The quasi-linear approximation has been used to calculate the turbulent fluxes, and it is successful to reproduce plasma profiles in some conditions [3]. On the other hand, some experiments have been suggested that the quasi-linear theory fails to explain the transport dynamics, e.g., the rapid propagation of cold pulse [4], the fast change of transport improvement before the local parameters changes [5,6], simultaneous inverse changes of temperature gradient across the transport barriers [7,8], and hysteresis in the flux-gradient and turbulence-gradient relations [9]. It is mentioned that some of these kinds of experiments, the edge cooling leads the sudden response of core temperature rise [10,11], was discussed by the quasi-linear approach [12]. However, the consistent answer to these various types of transport phenomena seems to be difficult for the quasi-linear approach alone.

To address on the above experimental observations, which are called as non-local transport phenomena [13], several theoretical models have been developed [14-16]. One of the concepts is known as the avalanching transport, which is exhibited in the self-organized criticality system [17-19]. When the local temperature exceeds the critical gradient, the excitation of instabilities relaxes the gradient and drives the transport to neighbors, causing to exceed the next critical gradient. The successive excitation of local transport events leads the propagation of heat and turbulence for long-radial distance with rapid propagation velocity [17]. The avalanching transport is commonly observed in gyrokinetic flux-driven simulations [20-23] and experiments [24-29]. In regard to the plasma confinement, the profile stiffness is possible to be explained by the presence of avalanching transport [20,21]. In the experiment on JT-60U, it was found that the avalanche-driven heat flux compensates the increase of NB power, which can lead to the constant temperature profile [26]. While profile stiffness is commonly observed in

tokamaks, it is not as prevalent in heliotron/stellarator devices. Thus, the search for avalanches in heliotron/stellarators is of significant concern and can be helpful in understanding the mechanism of profile stiffness observed in tokamaks.

In this paper, we present the observation of avalanche-like electron heat transport in helical device, Heliotron J. The deuterium plasma is generated by the ECH, and the power degradation is found in the ECH power scan experiments. The electron heat avalanches are detected by ECE radiometer using GHz sampling oscilloscope, which enables to set the bandwidth of intermediate frequency (IF) signals after the measurement. The characteristics of avalanches in steady state heliotron plasmas are studied for the first time, and its impact on the profile formation is discussed. The paper is organized as follows. In the section 2, the experimental setup including the newly developed ECE detection system is described. The observation of electron heat avalanches, their statistical characters, and the impact on SOL regime, are presented in the section 3. Finally, we discuss and summarized the paper in the section 4 and 5.

2. Experimental Setup

Heliotron J is a medium-sized helical-axis heliotron device, which can operate in flexible magnetic configurations by changing the current ratio among an helical coil and 2 types of toroidal coils, and 2 types of vertical coils. In this experiment, the deuterium plasmas are sustained in the standard magnetic field configuration with an averaged major radius of R = 1.2 m, an averaged minor radius of a = 0.17 m and a magnetic field strength at the magnetic axis of B = 1.25 T. The standard configuration is an optimized configuration, which can simultaneously achieve the reduction of the neo-classical ripple transport and generation of magnetic well for stabilizing MHD instabilities [30]. The rotational transform at the magnetic axis is 0.56, and it is almost constant in the whole plasma regime. A 2nd harmonics X-mode 70 GHz ECH is launched to produce deuterium plasmas, and the power of ECH is scanned from 113 kW to 287 kW for investigating the confinement properties of Heliotron J plasmas.

Figure 1 shows the ECH power (P_{ECH}) dependence of plasma stored energy (W_p), which is measured by a diamagnetic loop coil. In the experiment, the line-

averaged electron density of $\bar{n}_e \sim 1.0 \times 10^{19}$ /m^3 is kept constant by controlling the gas-puffing. In spite of P_{ECH} increase, the W_p hardly increases, which indicates the power degradation. The fitting curve shows the $W_p \propto P_{ECH}^{0.3}$ dependence, implying $\tau_E \approx W_p/P \propto P_{ECH}^{-0.7}$. The feature of power degradation can be found from the plasma profiles. As shown in Fig. 2(a), the power deposition of ECH is calculated by the lay-tracing code, TRAVIS [31]. Although the power of ECH increases, the electron temperature (T_e) profile is almost identical (Fig. 2(b)). This seems to be similar to the situation of stiffness found in tokamaks [26]. The condition of stiffness in tokamaks and heliotron/stellarators will be discussed in section 4. The flat to hollow electron density (n_e) profile shown in Fig. 2(c) is frequently observed in ECH plasmas in heliotron/stellarator [32].

Note that the power degradation can be considered as the result of cross-field transport. Figure 3 shows the discharge waveform of this experiment. As shown in Fig. 3(a) and (b), when the $\bar{n}_e$ approaches 1.0×10^{19} /m^3, the diamagnetic stored energy reaches a similar value, regardless of the heating power. At this time ($t \sim 0.275$ s), absolute extreme ultraviolet (AXUV) signals, which are observed along the line of sight directed towards the core region (Fig. 3(c)), exhibit similar values across different discharges, in comparison to the AXUV signals obtained from edge viewing (Fig. 3(d)). This result indicates that the radiation loss in the core regime is not the factor for the power degradation. The cross-field electron heat transport, mainly driven by anomalous components [33], is considered as the dominant process contributing to the power degradation in Heliotron J.

In this work, the electron temperature fluctuation is observed by the ECE radiometer of two detection system. The detection system is composed of the conventional filter bank with diode detector [34] and newly installed GHz sampling digital storage oscilloscope (DSO) [35]. The latter directly samples the intermediate frequency (IF) signal after the down conversion of broad radio frequency (RF) signal at f = 56-70 GHz. The sampling frequency and analog bandwidth of the DSO are 20 GHz and 8 GHz, respectively. Thus, the DSO is used to measure the IF of f = 0-8 GHz components simultaneously, which account for RF of f = 56-64 GHz. This is equivalent to measure the ECE signal at $\rho \sim 0.55$-

1.0, where ρ indicates normalized minor radius. The advantage of this new ECE detection system is that the IF filter bandwidth (B_{IF}) and video bandwidth (B_{vid}) can be selected after the data acquisition. Therefore, the time and radial resolution can be adjusted, which has a trade-off relationship with the thermal noise.

3. Experimental results

In this section, the experimental observations of electron temperature perturbations are presented. The GHz sampling DSO is used to discuss the propagation of T_e perturbations in section 3.1. The conventional filter bank ECE detection system is used to discuss the statistical feature of T_e perturbations in a whole plasma regime in section 3.2. The impact of T_e perturbations on the SOL regime is described in section 3.3.

3.1. Radial propagation of T_e perturbations

Figure 4 shows the time evolution of normalized electron temperature fluctuations $\tilde{T}_e/\bar{T}_e$, which have been low-pass filtered at 2 kHz, and rescaled and added offset to represent each measurement location. Here, the temperature fluctuations are obtained by setting B_{IF} = 0.3 GHz and B_{vid} = 0.5 MHz, respectively. As seen in Fig. 4(a)-(c), it can be seen that bumps and voids with a similar shape are observed over a long radial distance, particularly emphasized within the shaded hatched region. In addition, the correlation length of bumps and voids seems to increase with the ECH power. To clarify the correlation, we have performed the cross-correlation analysis on the electron temperature fluctuations obtained by setting B_{IF} = 0.4 GHz and B_{vid} = 0.5 MHz. Figure 5 shows the result of cross-correlation function (CCF) analysis, whose reference point is selected at $\rho \sim 0.55$. As the ECH power increases, the cross-correlation increases and extends toward the edge. Furthermore, a finite time lag can be seen from the core to the edge region, which indicates the radial propagation of T_e perturbations.

Figure 6 represents the peak value of CCF and corresponding time lag. The noise floor of CCF is determined by the root-mean-squared value of the CCF, excluding the region around the peak. To determine the propagation velocity, a

least squares fitting is performed within the range of $0.55 < \rho < 0.8$, where the CCF exceeds the noise floor. In the case of P_{ECH} = 113 kW discharge, the least squares fitting dose not converge because of the large error bar and a small time lag. The fitting is converged in the case of P_{ECH} = 192 kW and 287 kW discharges, and it can provide the estimation of outward propagation velocity of 0.39 ± 0.08 km/s and 0.63 ± 0.10 km/s, respectively. This is comparable to the ion diamagnetic drift velocity of ~0.8 km/s, which is similar to the observations in the flux-driven simulations [22]. Therefore, the T_e perturbation is considered as an avalanching transport.

The estimated propagation velocity of T_e perturbation is much faster than the time scale of diffusive transport. The effective thermal diffusion coefficient, $\chi_e^{avalanche}$, is evaluated as $\chi_e^{avalanche} = \Delta r^2/\Delta\tau$, where Δr and $\Delta\tau$ are the radial distance and time lag obtained from the CCF analysis. The result is compared to the thermal diffusion coefficient obtained by the power balance analysis (χ_e^{PB}), which is shown in Fig. 7. Here, the $\chi_e^{avalanche}$ is estimated by calculating CCF for every 9 points in the radial direction, and we neglect the sink terms in the power balance analysis, such as radiation loss and electron-ion equipartition. Apparently, the $\chi_e^{avalanche}$ is much larger than χ_e^{PB}, and thus it is suggested that the rapid transport phenomena observed in the transient experiments [4] could be explained by the dynamics of rapidly propagating avalanches.

Note that $\chi_e^{avalanche}$ reflects the spreading of a heat perturbation in terms of length and time, but it does not involve the energy information. Therefore, in order to discuss the impact of avalanching transport, it is necessary to estimate the heat flux directly. It was provided in Ref. [26] by using conditional averaging technique. In this work, we have deduced the avalanche-driven heat flux through a simple calculation. In the case of P_{ECH} = 287 kW discharge, the surface integral of avalanche-driven heat flux Q at ρ = 0.6 is, $Q \sim n_e \left(\frac{\tilde{T}_e}{\bar{T}_e}\right) \bar{T}_e v_r A \approx (1.0 \times 10^{19}\ m^{-3}) \cdot (0.04) \cdot (500\ eV) \cdot (600\ m/s) \cdot (4.5\ m^2) \approx 87\ kW$, where A indicate the plasma surface. Here, $\tilde{T}_e/\bar{T}_e \sim 4\%$ is estimated as the maximum

amplitude observed during avalanching events. The evaluated $Q{\sim}87\ kW$ accounts for approximately one-third of the input heating power, P_{ECH} = 287 kW. Thus, it is suggested that the significant amount of transport could be driven by avalanches.

3.2. Statistical feature of T_e perturbations

To clalyfy the characteristics of avalanches, the power spectrum analysis and the Hurst exponent has been investigated in the electron temperature fluctuations. The frequency power spectrum can reveal the self-similar behavior of avalanches, which is associated with a power-law scaling spectrum. As shown in Fig. 8(a), the power spectrum density (PSD) of ECE obtained at $\rho \sim 0.75$ indicate the power-law scaling, $PSD \propto f^{\alpha}$, in the frequency range of $0.1\ kHz < f < 2\ kHz$. In this case, the power-law coefficient α takes around -1, which indicates the self-similar characteristic of T_e perturbation. The self-similarity refers to the behavior of transport events exhibiting similarity across all scales, indicating that smaller avalanche events occur more frequently than larger ones. Note that the slope of power-law scaling increases (α decreases) with heating power. The Hurst exponent, which characterizes the correlation of the fluctuation in the time domain, is estimated using the rescaled range (R/S) analysis [17,18]. The Hurst exponent (H) can be derived by the slope of logarithmic plot of R/S value as, $[R/S] \propto \tau^{H}$, where τ indicate the time lag that characterizes the time scale of fluctuations. As shown in Fig. 8(b), the slope of R/S increases with heating power in the range of $0.5\ ms < \tau < 10\ ms$, which corresponds to the power-law regime in the frequency spectrum. The Hurst exponent approaches to 1 in the largest heating power, which indicates that the T_e perturbation has a long-time memory in the time domain. The persistent dynamics is one of the characters of avalanches.

Figure 9(a)-(c) shows the radial profiles of time-averaged amplitude of avalanche components ($f < 2\ kHz$), power-law scaling coefficient α and Hurst exponent H. As shown in Fig. 9(a), the amplitude of avalanches is large at the ECH deposition region, and it reflects the magnitude of heating power. Outside of the ECH deposition region, the amplitude of avalanches is approximately equivalent

in the radial direction for the case of the P_{ECH} = 113 kW and 287 kW discharges. On the other hand, the amplitude of avalanches slightly decreases in the radial direction for the case of the P_{ECH} = 192 kW and 247 kW discharges. Corresponding to the features of amplitude, α and H also change inside and outside of the ECH deposition region. As shown in Fig. 9(b) and (c), α and H inside the ECH deposition take ~ -1 and ~ 0.9, excluding P_{ECH} = 113 kW discharge. For the case of the P_{ECH} = 287 kW discharge, α and H take values of approximately -1.2 and 1 at the outside of the ECH deposition region. This indicates that the avalanches are active outside of the source region in the case of high heating. For the case of the P_{ECH} = 192 kW and 247 kW discharges, α and H increase and decrease towards the edge region, which indicate the degradation of avalanches outside of the source region. The result is consistent with the CCF analysis, which shows an increase in the radial correlation length of avalanches with increasing heating power.

3.3. The relation to the SOL regime

Up to this point, we have investigated the electron heat avalanches using ECE diagnostics. In this subsection, using D_α emission signal, we study the influence of avalanches in the SOL regime. Figure 10 shows the frequency power spectrum of D_α emission, which exhibited with *1/f* power-law scaling. The magnitude of *1/f* power-law region is above the noise level that is deduced by the signal without the plasma (gray line). The slope of power-law scaling is slightly increased with the increases of heating power. Note that the D_α emission is obtained with a line of sight directed towards the core, rather than across the SOL regime. Thus, the line integration effect of the D_α emission is minimum. The *1/f* power-law region extends at $0.2\ kHz < f < 10\ kHz$, which is wider than that observed in the ECE. This is because the ECE measurements are strongly suffered by thermal noise, as indicated by the dashed line in Fig. 8(a). This suggests that the amplitude of electron heat avalanches could be larger than our estimate, and the contribution of avalanche-driven electron heat flux could be more significant.

It is found that the electron heat avalanches have a finite correlation to the D_α emission, which is mainly contributed by the electron density driven by particle

flux. Figure 11(a) shows the CCF between ECE ($\rho \sim 0.95$) and D_α emission, both of which have been low-pass filtered at 2 kHz. Because the error bar of the CCF is large, the convergence study of CCF is provided. As shown in Fig. 11(b), the *1/N* dependence of the CCF indicates that the CCF will converge to a finite value that exceeds the noise floor, except for the P_{ECH} = 113 kW case. Here, *N* indicates the ensemble average. The negative correlation observed between the ECE and D_α emission is similar to the situation seen in the edge localized mode (ELM) [36]. It should be noted that a finite negative correlation is similarly observed between ECE and D_α emission at four different toroidal locations. Furthermore, the time lags of the negative correlation peaks are equivalent, indicating that the T_e perturbation occurs simultaneously in the toroidal direction. Thus, the T_e perturbation is considered as a transport event, characterized as the avalanche.

The CCF between ECE and D_α emission is investigated at different radial position of ECE measurements. Figure 12 shows the radial profiles of absolute value of maximum CCF between ECE and D_α emission. While the CCF in the ECH deposition region is below the noise floor, a finite correlation can be observed outside the source region. The absolute value of the CCF increases with the higher heating power. The result suggest that the enhanced electron heat avalanches can propagate to the SOL regime and interact with the particle transport.

4. Discussion

First, the impact of avalanching transport on the formation of stiffness profile is discussed. In this study, we have found that (i) avalanche driven electron heat flux could be significant and comparable to the input heating power, (ii) avalanches become dominant with the increase of the heating power, and (iii) avalanches expand towards the outside of the source region that can extend to the whole plasma regime. Note that the last part is also suggested during the power degradation study in TJ-II [37]. These findings could provide a potential explanation to the problem that the electron temperature hardly increases against the heating power, as shown in Fig. 2(b). The significance of avalanching transport

on the formation of the resilient temperature profile is also reported in tokamak, JT-60U [26]. The response of the temperature profile in both Heliotron J and JT-60U shows a similar trend, i.e., the electron temperature profile hardly changes against the increases of the on-axis heating.

Looking back on the past, the presence of stiffness was confirmed in tokamaks in the off-axis heating [38]. The scale length of the temperature gradient is unchanged against the location of the heating deposition. On the other hand, the temperature profile is easily changed against the off-axis heating in heliotron/stellarator [32]. However, when the presence of a finite on-axis heating, the temperature profile against the off-axis heating is similar to the pure on-axis heating case [32]. This is an interesting indication of stiffness in heliotron/stellarator suggested by U. Stroth [39]. Due to the ohmic current heating, the condition of heating source is different between in heliotron/stellarators and tokamaks. The broad central heating always exists in tokamaks. As shown in this work, the avalanching transport is strongly influenced by the power and location of the heating source. As discussed in the sandpile simulation [40], the uphill avalanching transport can occur in the dominant off-axis heating situation, which could potentially produce the peak temperature profile. It could be considered that the difference of heating source deposition could influence on the avalanching transport that potentially cause the different profile response between heliotron/stellarators and tokamaks. To clarify this assumption, the off-axis heating experiment is planned for the future work.

Next, we discuss about the influence of the electron heat avalanches on the SOL region. Controlling the SOL width has been paid attention for heat load mitigation on the divertor, which is one of the key challenges to achieve a fusion power plant. Here, the non-local feature of turbulence, which can propagate from the edge to the SOL, has been considered a key factor in determining the SOL width [41,42]. In our study, the enhanced avalanching electron heat transport correlates to the D_α emission in the SOL, which suggests the penetration of avalanches into the SOL region. The other evidence can be seen in Fig. 13. As heating power increases, the correlation of T_e perturbation between the core and

SOL can be finite. Note that the optical depth of ECE in the SOL region is thin, however, the condition of optical depth is equivalent in every discharges. It has been reported that the exponential power decay length of SOL is strongly correlated to the pedestal gradient [43]. In this sense, it is interesting to investigate how avalanching transport, which can connect the core, edge, and SOL transport, influences the pedestal structure and SOL width.

Finally, we mention about the coupling between the electron heat and particle transport, which is suggested by the finite correlation between ECE and D_α emission. In the ECH plasmas, the hollow density profile is frequently found in heliotron/stellarators. It has been studied that the convective particle flux is not fully explained by the neo classical transport [32,44]. It is interesting to consider the avalanching transport, which could contribute to the particle flux as a convective term. The trend of increased core heating and its effect on enhancing convective particle fluxes is also of interest [32].

5. Summary

In summary, we observed the presence of electron heat avalanches during the power degradation in Heliotron J plasmas. The T_e perturbation measured by the ECE exhibits several characteristics, including: (i) propagation from the core to the edge with a radial velocity comparable to the diamagnetic drift velocity, (ii) a frequency spectrum contains a *1/f* power-law scaling and a Hurst exponent close to 1, and (iii) it is dominant in the ECH deposition region and spreads to the edge region as the heating power increases. The propagation velocity of avalanches is much faster than the diffusive transport, which could drive the significant amount of electron heat flux. The impact of avalanches on the stiffness profiles is discussed. The finite correlation between the ECE and the D_α emission indicates that the avalanches also impact to the SOL plasmas and particle fluxes, which are interesting aspects found in this study.

Acknowledgement

The authors appreciate to Heliotron J team for their strong supports. The authors thank to the members of the Asia Pacific Transport Working Group 2023 for fruitful discussions and comments. This work is partly supported by the Grant-in-Aid for Scientific Research of JSPS, Japan (23K13084) and JSPS Core-to-Core Program, 'PLADys'.

Reference

[1] E. J. Doyle *et al.*, Chapter 2: Plasma confinement and transport. *Nucl. Fusion* **47**, S18 (2007).

[2] H. Yamada *et al.*, Characterization of energy confinement in net-current free plasmas using the extended International Stellarator Database. *Nucl. Fusion* **45**, 1684 (2005).

[3] G. M. Staebler, J. E. Kinsey and R. E. Waltz, A theory-based transport model with comprehensive physics. *Phys. Plasmas* **14**, 055909 (2007).

[4] B. P. van Milligen *et al.*, Ballistic transport phenomena in TJ-II. *Nucl. Fusion* **42**, 787 (2002).

[5] U. Stroth, L. Giannone, H.-J. Hartfuss, the ECH Group and the W7-AS Team, Fast transport changes and power degradation in the W7-AS stellarator U. *Plasma Phys. Control. Fusion* **38**, 611 (1996).

[6] T. Kobayashi *et al.*, Prompt core confinement improvement across the L–H transition in DIII-D: Profile stiffness, turbulence dynamics, and isotope effect Cite. *Phys. Plasmas* **30**, 032301 (2023).

[7] K. Ida *et al.*, Transition between Internal Transport Barriers with Different Temperature-Profile Curvatures in JT-60U Tokamak Plasmas. *Phys. Rev. Lett.* **101**, 055003 (2008).

[8] D. L. Yu *et al.*, Ion internal transport barrier in neutral beam heated plasmas on HL-2A. *Nucl. Fusion* **56**, 056003 (2016).

[9] S. Inagaki, *et al.*, How is turbulence intensity determined by macroscopic variables in a toroidal plasma? *Nucl. Fusion* **53**, 113006 (2013).

[10] K. W. Gentle, *et al.*, Strong Nonlocal Effects in a Tokamak Perturbative Transport Experiment. *Phys. Rev. Lett.* **74**, 3620 (1995).

[11] N. Tamura, *et al.,* Impact of nonlocal electron heat transport on the high temperature plasmas of LHD. *Nucl. Fusion* **47**, 449 (2007).

[12] P. Rodriguez-Fernandez, *et al.,* Explaining Cold-Pulse Dynamics in Tokamak Plasmas Using Local Turbulent Transport Models. *Phys. Rev. Lett.* **120**, 075001 (2018).

[13] K. Ida, *et al.,* Towards an emerging understanding of non-locality phenomena and non-local transport. *Nucl. Fusion* **55**, 013022 (2015).

[14] P. Beyer, S. Benkadda, X. Garbet and P. H. Diamond, Nondiffusive Transport

in Tokamaks: Three-Dimensional Structure of Bursts and the Role of Zonal Flows. *Phys. Rev. Lett.* **85**, 4892 (2000).
[15] K. Itoh, *et al.*, Hysteresis and fast timescales in transport relations of toroidal plasmas. *Nucl. Fusion* **57**, 102012 (2017).
[16] R. O. Dendy, S. C. Chapman and S. Inagaki, Modelling the measured local time evolution of strongly nonlinear heat pulses in the Large Helical Device. *Plasma Phys. Control. Fusion* **55**, 115009 (2013).
[17] T. S. Hahm and P. H. Diamond, Mesoscopic Transport Events and the Breakdown of Fick's Law for Turbulent Fluxes. *J. Kor. Phys. Soc.* **73**, 747 (2018).
[18] R. Sanchez and D. E. Newman, Self-organized criticality and the dynamics of near-marginal turbulent transport in magnetically confined fusion plasmas. *Plasma Phys. Control. Fusion* **57**, 123002 (2015).
[19] G. Dif-Pradalier, *et al.,* The E×B staircase of magnetised plasmas. *Nucl. Fusion* **57**, 066026 (2017).
[20] Y. Idomura, H. Urano, N. Aiba and S. Tokuda, Study of ion turbulent transport and profile formations using global gyrokinetic full-*f* Vlasov simulation. *Nucl. Fusion* **49**, 065029 (2009).
[21] S. Ku, C. S. Chang and P. H. Diamond, Full-f gyrokinetic particle simulation of centrally heated global ITG turbulence from magnetic axis to edge pedestal top in a realistic tokamak geometry. *Nucl. Fusion* **49**, 115021 (2009).
[22] Y. Sarazin, *et al.,* Large scale dynamics in flux driven gyrokinetic turbulence. *Nucl. Fusion* **50**, 054004 (2010).
[23] W. Wang, Y. Kishimoto, K. Imadera, J. Q. Li and Z. X. Wang, A mechanism for the formation and sustainment of the self-organized global profile and E × B staircase in tokamak plasmas. *Nucl. Fusion* **58**, 056005 (2018).
[24] P. A. Politzer, Observation of Avalanchelike Phenomena in a Magnetically Confined Plasma. *Phys. Rev. Lett.* **84**, 1192 (2000).
[25] M. J. Choi *et al.*, Experimental observation of the non-diffusive avalanche-like electron heat transport events and their dynamical interaction with the shear flow structure. *Nucl. Fusion* **59**, 086027 (2019).
[26] F. Kin *et al.*, Experimental evaluation of avalanche type of transport in magnetic confinement plasmas. *Nucl. Fusion* **63**, 016015 (2023).

[27] W. Chen *et al.*, Avalanche electron heat transport events triggered by non-linear mode couplings in HL-2A neutral beam injection heated L-mode plasmas. *Nucl. Fusion* **60**, 094003 (2020).
[28] B. Van Compernolle, G. J. Morales, J. E. Maggs and R. D. Sydora, Laboratory study of avalanches in magnetized plasmas. *Phys. Rev. E* **91**, 031102 (2015).
[29] N. Kenmochi *et al.*, Preceding propagation of turbulence pulses at avalanche events in a magnetically confined plasma. *Sci. Rep.* **12**, 6979 (2022).
[30] M. Wakatani *et al.*, Study of a helical axis heliotron. *Nucl. Fusion* **40**, 569 (2000).
[31] N.B. Marushchenko, Y. Turkin and H. Maassberg, Ray-tracing code TRAVIS for ECR heating, EC current drive and ECE diagnostic, *Comput. Phys. Commun.* **185** 165 (2014).
[32] U. Stroth *et al.*, Evidence for Convective Inward Particle Transport in a Stellarator. *Phys. Rev. Lett.* **82**, 928 (1999).
[33] N. Kenmochi *et al.*, Characteristics of electron internal transport barrier in Heliotron J. *Plasma Phys. Control. Fusion* **59**, 055013 (2017).
[34] M. Luo *et al.*, Measurement of Electron Temperature Profile and Fluctuation with ECE Radiometer System in Heliotron J. *Plasma Fusion Res.* **15**, 2402038 (2020).
[35] H. Tsuchiya, S. Inagaki, T. Tokuzawa, N. Tamura and Y. Nagayama, Digital Correlation ECE Measurement Technique with a Gigahertz Sampling Digitizer, *Plasma Fusion Res.* **9**, 3402021 (2014).
[36] K. Kamiya *et al.*, Edge localized modes: recent experimental findings and related issues. *Plasma Phys. Control. Fusion* **49**, S43 (2007).
[37] B. Ph. van Milligen, B. A. Carreras, C. Hidalgo, A. Cappa and TJ-II Team, A possible mechanism for confinement power degradation in the TJ-II stellarator. *Phys. Plasmas* **25**, 062503 (2018).
[38] C. C. Petty and T. C. Luce, Inward transport of energy during off-axis heating on the DIII-D tokamak. *Nucl. Fusion* **34**, 121 (1994).
[39] U. Stroth, A comparative study of transport in stellarators and tokamaks. *Plasma Phys. Control. Fusion* **40**, 9 (1998).
[40] T. K. March, S. C. Chapman, R. O. Dendy and J. A. Merrifield, Off-axis electron cyclotron heating and the sandpile paradigm for transport in tokamak

plasmas. *Phys. Plasmas* **11**, 659 (2004).
[41] G. Grenfell, *et al.*, Measurement and control of turbulence spreading in the scrape-off layer of TJ-II stellarator. *Nucl. Fusion* **59**, 016018 (2019).
[42] M. Kobayashi *et al.*, Turbulence Spreading into an Edge Stochastic Magnetic Layer Induced by Magnetic Fluctuation and Its Impact on Divertor Heat Load. *Phys. Rev. Lett.* **128**, 125001 (2022).
[43] D. Silvagni *et al.*, Scrape-off layer (SOL) power width scaling and correlation between SOL and pedestal gradients across L, I and H-mode plasmas at ASDEX Upgrade. *Plasma Phys. Control. Fusion* **62**, 045015 (2022).
[44] K. Tanaka *et al.*, Experimental study of particle transport and density fluctuations in LHD. *Nucl. Fusion* **46**, 110 (2006).

Figures

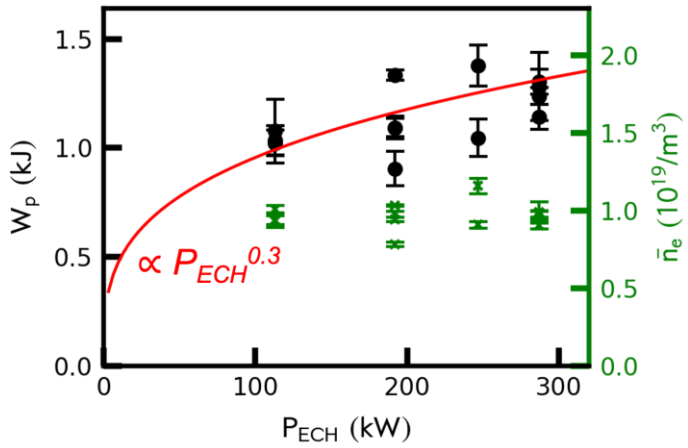

Fig. 1. P_{ECH} dependence of the diamagnetic stored energy (W_p) and line-averaged electron density ($\bar{n}_e$).

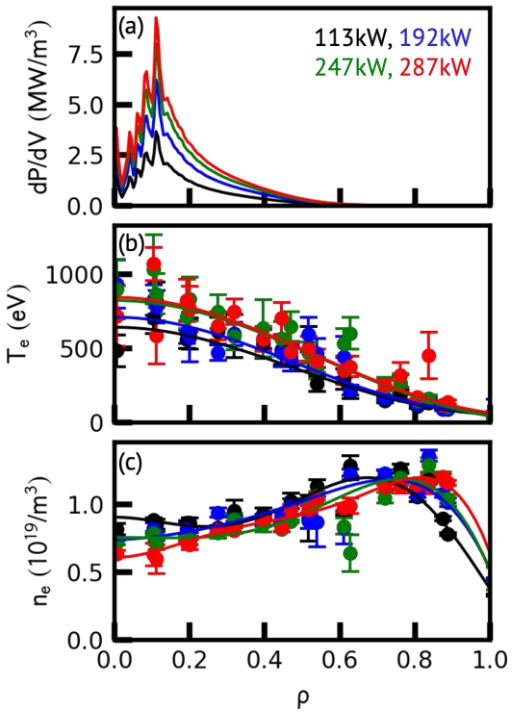

Fig. 2 Radial profiles of (a) ECH deposition calculated by the TRAVIS, (b) electron temperature and (c) electron density measured by Thomson scattering diagnostics.

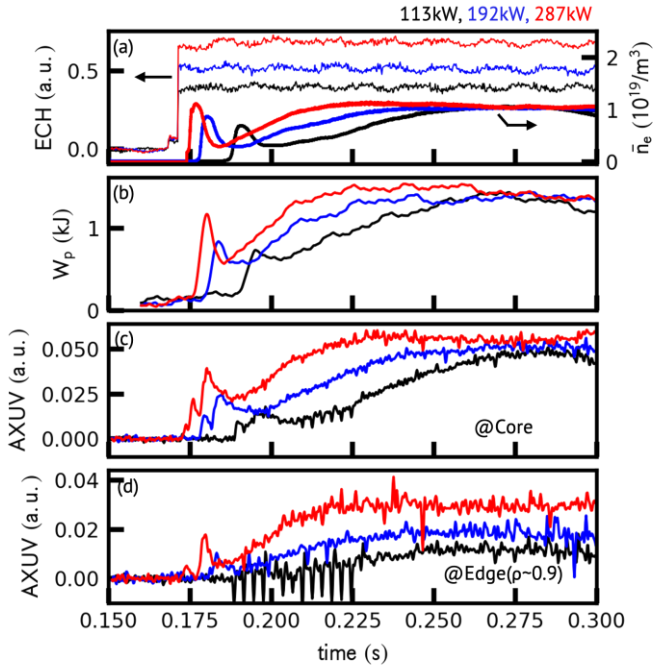

Fig. 3 Discharge waveforms of (a) power of ECH injection and line-averaged electron density, (b) diamagnetic stored energy, and AXUV signals with line of sight directed towards (c) core and (d) edge region.

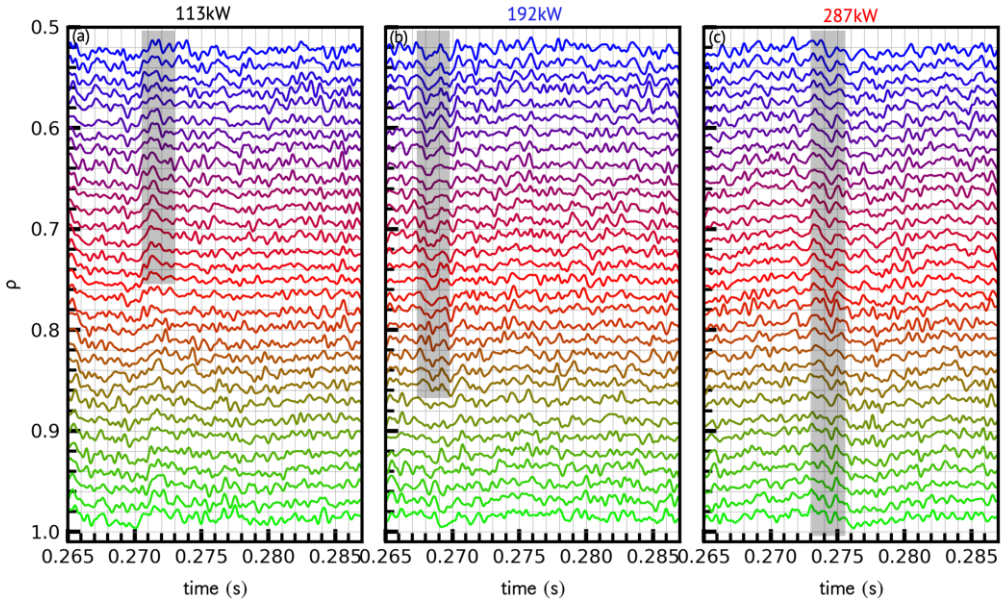

Fig. 4 Heating power dependency of spatio-temporal evolution of normalized electron temperature fluctuations ($\frac{\tilde{T}_e}{\bar{T}_e}$), which are arranged as $\frac{\tilde{T}_e}{\bar{T}_e} + \rho$, where ρ indicates the normalized minor radius of each position of ECE measurement.

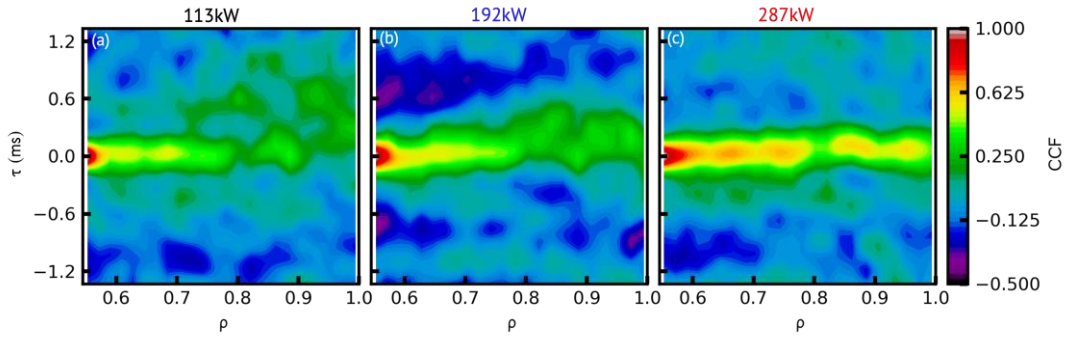

Fig. 5 The spatio-temporal evolution of cross-correlation function (CCF) of T_e perturbation. The reference point of CCF analysis is $\rho \sim 0.55$.

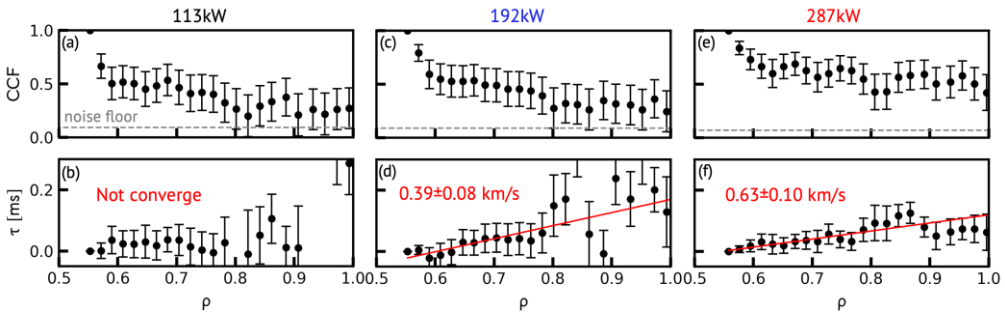

Fig. 6 The radial profiles of (a), (c), (e) peak value of CCF and (b), (d), (f) corresponding time lag. The least squares fitting is tried on the time lag plot at $0.55 < \rho < 0.8$ and the results are shown in the red line.

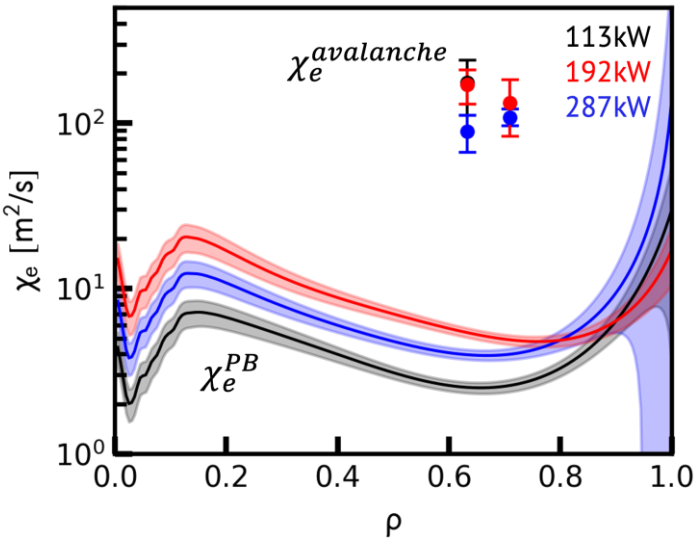

Fig. 7 The radial profiles of effective thermal diffusive coefficient of avalanches ($\chi_e^{avalanche}$) and thermal diffusive coefficient derived by the power balance (χ_e^{PB}).

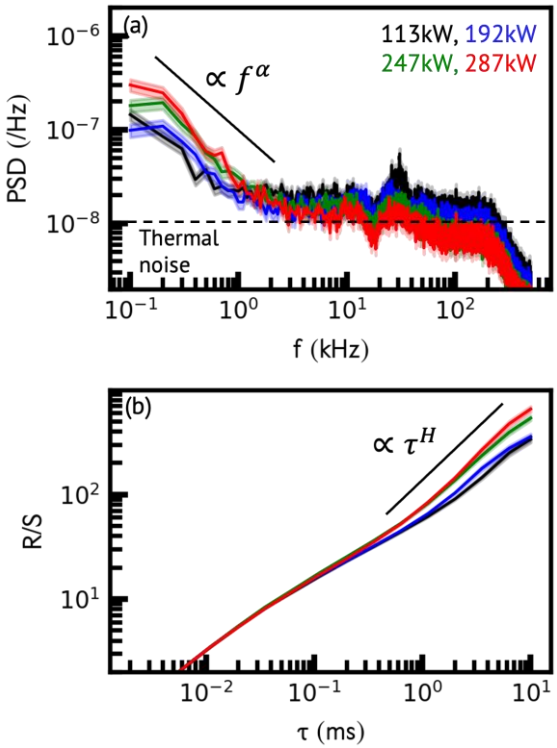

Fig. 8 (a) Frequency spectrum of normalized T_e fluctuations measured by ECE diagnostics. (b) R/S analysis of normalized T_e fluctuations. The T_e fluctuations at $\rho \sim 0.75$ are used for the analysis.

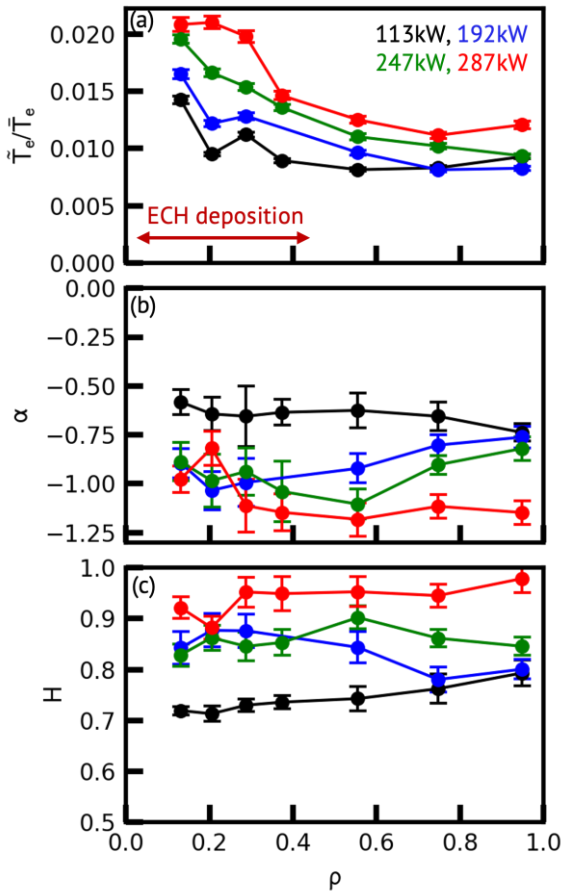

Fig. 9 Radial profiles of (a) time-averaged amplitude of avalanche components of T_e fluctuations ($f < 2\ kHz$), (b) power-law scaling coefficient α of a frequency spectrum ($PSD \propto f^{\alpha}$), and (c) Hurst exponent H.

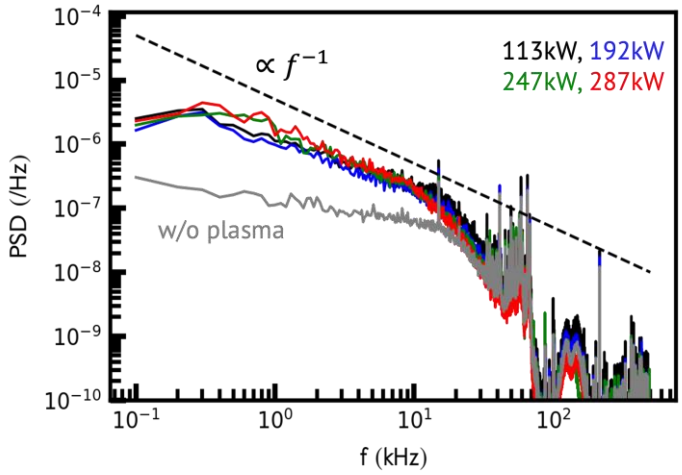

Fig. 10 Frequency spectrum of D_α emission.

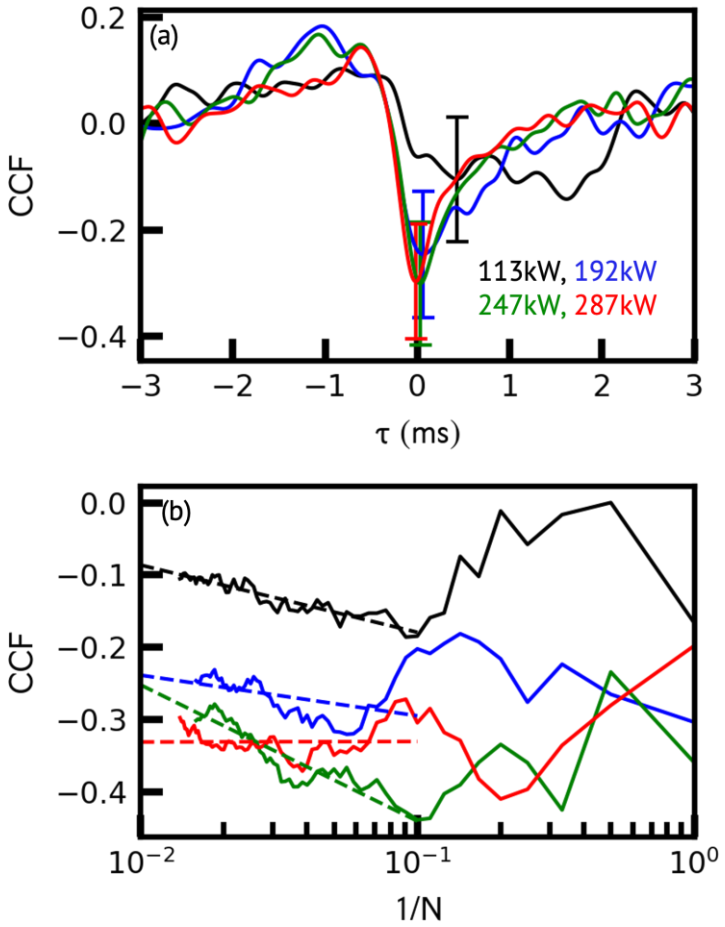

Fig. 11 (a) The CCF between ECE at $\rho \sim 0.95$ and D_α emission. Both of the signals are low-pass filtered at 2 kHz. (b) The convergence study of peak value of the CCF, where N indicates the ensemble average.

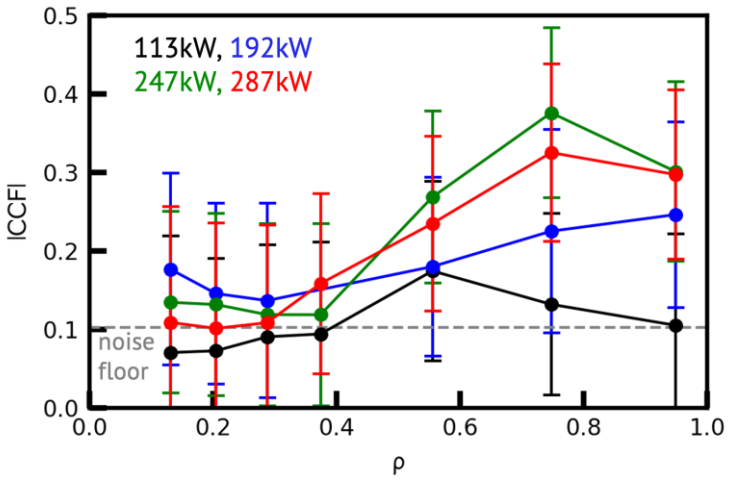

Fig. 12 The absolute value of maximum CCF between ECE measured at different radial positions and D_α emission.

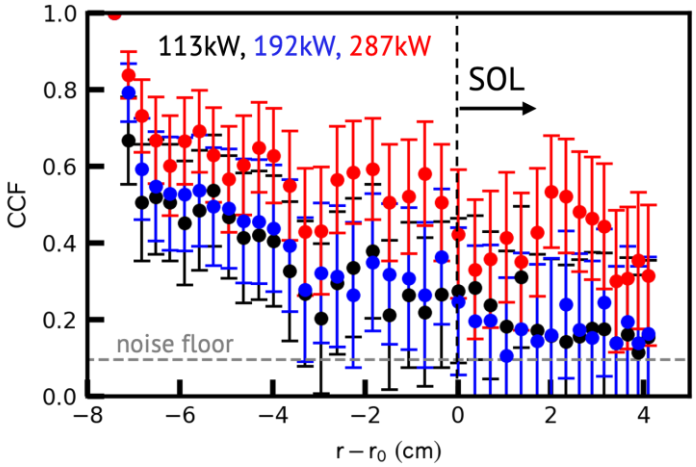

Fig. 13 Radial profiles of CCF of ECE including the SOL region. The reference point of CCF is r - r_0 ~ -7.5 cm, which is equivalent at ρ ~ 0.55.